LETTER

Mapping the optimal route between two quantum states

S. J. Weber[1], A. Chantasri[2], J. Dressel[3], A. N. Jordan[2,4], K. W. Murch[5] & I. Siddiqi[1]

A central feature of quantum mechanics is that a measurement result is intrinsically probabilistic. Consequently, continuously monitoring a quantum system will randomly perturb its natural unitary evolution. The ability to control a quantum system in the presence of these fluctuations is of increasing importance in quantum information processing and finds application in fields ranging from nuclear magnetic resonance[1] to chemical synthesis[2]. A detailed understanding of this stochastic evolution is essential for the development of optimized control methods. Here we reconstruct the individual quantum trajectories[3–5] of a superconducting circuit that evolves under the competing influences of continuous weak measurement and Rabi drive. By tracking individual trajectories that evolve between any chosen initial and final states, we can deduce the most probable path through quantum state space. These pre- and post-selected quantum trajectories also reveal the optimal detector signal in the form of a smooth, time-continuous function that connects the desired boundary conditions. Our investigation reveals the rich interplay between measurement dynamics, typically associated with wavefunction collapse, and unitary evolution of the quantum state as described by the Schrödinger equation. These results and the underlying theory[6], based on a principle of least action, reveal the optimal route from initial to final states, and may inform new quantum control methods for state steering and information processing.

Our experiment focuses on the dynamics of two quantum levels of a superconducting circuit (a quantum bit, or qubit), which can be continuously measured and excited by microwave pulses. To access individual quantum trajectories, we make use of the fact that fully projective measurement (or wavefunction collapse) happens over an average time-scale τ controlled by the interaction strength between the system and the detector. By recording the measurement signal with high fidelity in time steps much shorter than τ, we realize a continuous sequence of weak measurements and track the qubit state as it evolves in a single experimental iteration. Individual weak measurements have been recently used in atomic physics experiments that probe wavefunction collapse[7] and demonstrate state stabilization[8]. In the domain of superconducting circuits, weak measurements[9] have only recently been realized, owing to the challenge associated with high-fidelity detection of microwave signals near the single-photon level. Advances in superconducting parametric amplifiers have enabled continuous feedback control[10–12], the observation of individual quantum trajectories[13,14], the determination of weak values[15,16] and the entanglement of qubits[17,18].

In previous work[13], we demonstrated the ability to track individual quantum trajectories using continuous quantum non-demolition weak measurement. To fully understand the nature of these trajectories, it is necessary to explore their statistical and dynamical properties. Here, by examining a large number of trajectories, we gain insight into the conditional dynamics of open quantum systems. We consider the subset of trajectories that end in a particular final state, which reveals the most probable path connecting two points in quantum state space. Furthermore, whereas previous work[13] considered only the case of continuous

measurement, we now introduce a concurrent drive at the qubit frequency, resulting in Rabi oscillations that turn qubit state populations into coherences, and vice versa. We are able to track quantum trajectories that exhibit dynamics associated with both measurement backaction and unitary evolution, and find that our theoretical formalism[6] quantitatively describes the family of trajectories that connect two points in quantum state space.

Our experiment consists of a superconducting transmon circuit[19] dispersively coupled to a waveguide cavity[20] (Fig. 1a). Considering only the two lowest levels of the transmon as a qubit, our system is described by the Hamiltonian $H = H_0 + H_{int} + H_R$, where

$$H_{int} = -\hbar\chi a^\dagger a \sigma_z$$

$$H_R = \hbar\frac{\Omega}{2}\sigma_y$$

and where H_0 describes the qubit and cavity energy and decay terms. Here $\hbar$ is the reduced Planck's constant, $a^\dagger$ and a are respectively the creation and annihilation operators for the cavity mode, and σ_y and σ_z are qubit Pauli operators. The Hamiltonian H_R describes a microwave drive at the qubit transition frequency, which induces unitary evolution of the qubit state characterized by the Rabi frequency Ω, and H_{int} is the interaction term, characterized by the dispersive coupling rate
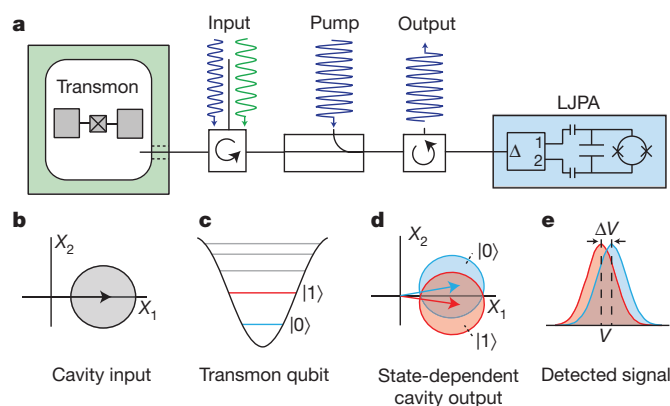
Figure 1 | Set-up. a, A transmon circuit is dispersively coupled to a three-dimensional copper waveguide cavity. Microwave signals that reflect off the cavity port are amplified by a lumped-element Josephson parametric amplifier[22] (LJPA) operating near the quantum limit. **b**, A microwave tone that probes the cavity near resonance is shown as a phasor in the X_1–X_2 plane, with zero-point quantum fluctuations shown by the shaded region. **c**, Ground and excited energy levels are shown on the transmon potential. **d**, The reflected microwave tone acquires a qubit-state-dependent phase shift that is smaller than the quantum fluctuations of the measurement signal. After further amplification, the X_2 quadrature of the measurement tone is digitized. **e**, The measurement is calibrated by examining the distributions of measurement signals for the qubit prepared in the $|0\rangle$ (blue) and $|1\rangle$ (red) states.

[1]Quantum Nanoelectronics Laboratory, Department of Physics, University of California, Berkeley, California 94720, USA. [2]Department of Physics and Astronomy and Center for Coherence and Quantum Optics, University of Rochester, Rochester, New York 14627, USA. [3]Department of Electrical Engineering, University of California, Riverside, California 92521, USA. [4]Institute for Quantum Studies, Chapman University, University Drive, Orange, California 92866, USA. [5]Department of Physics, Washington University, St Louis, Missouri 63130, USA.
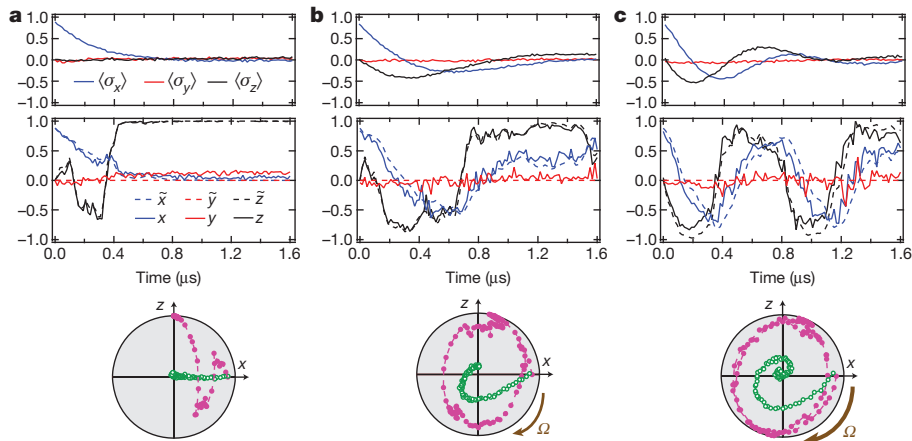
Figure 2 | Quantum trajectories of the quantum state on the Bloch sphere are plotted against time. The upper panels depict the full ensemble evolution. The middle panels depict individual quantum trajectories (dashed curves), with comparison with their tomographic reconstructions (solid curves). At the bottom, we plot individual trajectories (magenta) and the ensemble averages (green) in the x–z plane of the Bloch sphere. **a–c** correspond to different values of the Rabi drive: $\Omega/2\pi = 0$ MHz (**a**), 0.56 MHz (**b**) and 1.08 MHz (**c**). Here $\tau = 315$ ns and $\Gamma = 3.85 \times 10^6$ s^{-1}.

$\chi/2\pi = -0.6$ MHz. This term describes a qubit-state-dependent frequency shift of the cavity, which we use to perform quantum state measurement in our system. We will work in a rotating frame to eliminate the precession of the Bloch vector from the energy level splitting of the qubit. As depicted in Fig. 1b–e, a microwave tone that probes the cavity near its resonance frequency will acquire a qubit-state-dependent phase shift. If the measurement tone is very weak, quantum fluctuations of the electromagnetic mode fundamentally obscure this phase shift, resulting in a partial or weak measurement of the qubit state. We use a near-quantum-limited parametric amplifier[21,22] to amplify the X_2 quadrature of the reflected signal, which is proportional to the qubit-state-dependent phase shift. After further amplification, we digitize the signal in 16 ns time steps, resulting in a measurement signal $V(t)$. Each time step is small compared with the characteristic measurement time, $\tau = \kappa/16\chi^2 \bar{n}\eta_{\mathrm{col}}\eta_{\mathrm{amp}}$, where $\bar{n}$ is the average intracavity photon number, $\kappa/2\pi = 9.0$ MHz is the cavity decay rate and $\eta_{\mathrm{col}}\eta_{\mathrm{amp}}$ is the measurement quantum efficiency[23], which decomposes into separate collection and amplification efficiencies. The characteristic measurement time τ is calibrated by examining (Gaussian) histograms of the measurement results for the qubit prepared in the σ_z eigenstates $|0\rangle$ and $|1\rangle$, and is defined by the time it takes to separate the two distributions by two standard deviations[24], $\Delta V = 2\sigma$.

In our experiment, we prepare the qubit in the positive eigenstate of the σ_x Pauli operator (along the x axis of the Bloch sphere), by first making a projective measurement along the z axis and then a $\pi/2$-rotation about the y axis[13]. By considering only the instances where the measurement result is found to be $|0\rangle$, we herald the preparation of a high-fidelity ground state. Then a measurement tone at 6.8316 GHz continuously probes the cavity for a variable time t, which weakly measures the qubit in the σ_z basis. Finally, we apply further rotations and perform a projective measurement to conduct quantum state tomography. In Fig. 2 (top panels), we show the ensemble-averaged tomography for three different Rabi drive strengths. From these curves, we extract $\Omega/2\pi = 0$, 0.56 and 1.08 MHz and the ensemble coherence decay rate Γ by comparison with theory as discussed in Methods. From Γ, we calculate a total quantum efficiency $\eta_{\mathrm{tot}} = 1/2\tau\Gamma = \eta_{\mathrm{col}}\eta_{\mathrm{amp}}\eta_{\mathrm{env}} = 0.4$, where the last factor indicates the (nearly negligible) extra environmental dephasing $\eta_{\mathrm{env}} = \left(1 + \kappa/8\chi^2\bar{n}T_2^*\right)^{-1}$, with $T_2^* = 15$ μs.

In each iteration of the experiment, we can use the recorded measurement signal to calculate the best estimate for the qubit state conditioned on the measurement record. As discussed in Methods, at each time step we apply a two-step update procedure to track the evolution of the system density matrix ρ. We account for the measurement result using a quantum generalization of Bayes' rule[23,24], and we account for the

Rabi drive by applying a unitary rotation. Our finite detector efficiency reflects our imperfect knowledge about the state of the system and results in a decay of coherence given by rate $\gamma = \Gamma - 1/2\tau$. From the density matrix ρ, we calculate expectation values of the Pauli operators conditioned on the measurement signal: $x \equiv \mathrm{tr}[\rho\sigma_x]$, $y \equiv \mathrm{tr}[\rho\sigma_y]$ and $z \equiv \mathrm{tr}[\rho\sigma_z]$ (the components of the Bloch vector).

In Fig. 2a, we display a sample trajectory with no drive ($\Omega = 0$) that shows the stochastic motion of the qubit state as it evolves under measurement and is ultimately projected into the $|0\rangle$ state. As described in Methods, we use conditioned quantum state tomography to reconstruct
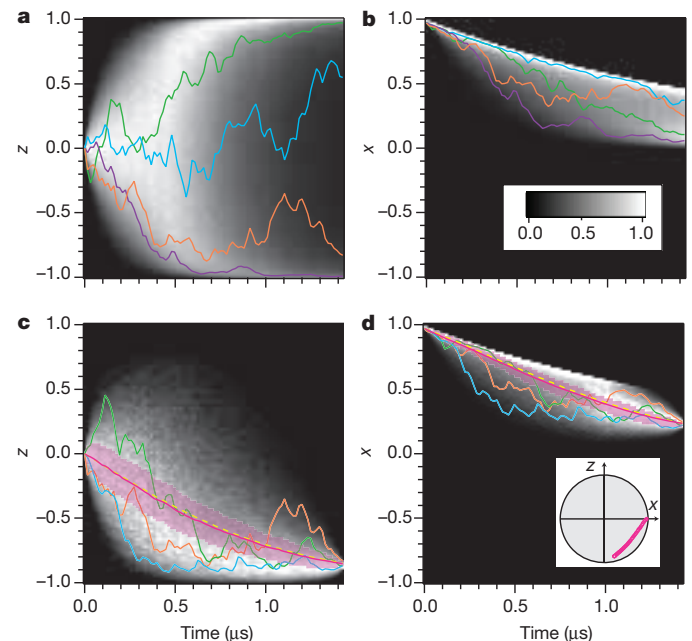
Figure 3 | Greyscale histograms of quantum trajectories in the undriven case. Measurement duration, 1.424 μs. **a, b**, Histograms of all measured z (**a**) and x (**b**) trajectories, beginning from state ($x_{\mathrm{I}} = 0.97$, $z_{\mathrm{I}} = 0$). Representative trajectories are shown in colour. **c, d**, Histograms of trajectories z (**c**) and x (**d**), conforming to the final chosen boundary condition, $z_{\mathrm{F}} = -0.85 \pm 0.03$. The most likely trajectories from the experimental data are shown as magenta curves, with their standard deviations shown by the magenta bands. The most likely paths in z and x predicted from the theory are shown as yellow dashed curves. Other representative trajectories are shown in other colours. Inset in **d**, the most likely trajectory is plotted on the x–z plane of the Bloch sphere. Here $\tau = 1.25$ μs and $\Gamma = 0.94 \times 10^6$ s^{-1}.

the trajectory. Figure 2b, c demonstrates that we can track the state faithfully in the presence of unitary state evolution induced by a drive at the qubit frequency. The drive induces Rabi oscillations while the system is being continuously measured. The resulting dynamics is fully quantum, going beyond the pure measurement case[13]. These trajectories highlight the stark difference between ensemble dynamics and the dynamics of individual quantum trajectories; whereas the ensemble average decays rapidly to a mixed state, the individual trajectories remain remarkably pure despite the modest quantum efficiency, $\eta_{tot} = 0.4$.

Using this ability to track individual trajectories starting from a given initial state, we now consider the sub-ensemble of trajectories that arrive at a particular final state at a given time. This sub-ensemble allows us to examine the conditional quantum dynamics of the state that satisfy two boundary conditions, one in the past ('pre-selection') and one in the future ('post-selection'). This is similar to an analysis that leads to 'weak values'[25-27], and time-continuous generalizations[16,28] that consider an additional projective post-selection measurement. In contrast to that approach, we use only a solitary continuous measurement: the pre-selection is just the initial state, and the post-selection is simply whatever the state is when the detector stops measuring. The resulting average of the measurement output gives a 'weak function' that connects the boundary conditions.

To investigate the full ensemble and post-selected sub-ensemble dynamics, we perform 10^5 iterations of the experiment with a measurement duration of 1.424 μs. For each experiment, we construct the quantum state trajectory by finding x and z for every time step. Figure 3 displays the measurement dynamics for $\Omega = 0$. We consider the sub-ensemble

of trajectories that have final values $(z(1.424\ \mu s), x(1.424\ \mu s))$ within 0.03 of $(x_F, z_F) = (-0.85, 0.23)$. This analysis allows us to examine properties of the conditional trajectories such as the most likely path that connects pre- and post-selected states.

The most likely paths can be theoretically calculated using a stochastic path integral representation of the joint probability of the measurement outcomes at every point in time with boundary condition constraints. The conditional detector backaction on the quantum state can be imposed at every time step with Lagrange multipliers (p_x, p_z) as auxiliary dynamical parameters. Finding the extremum of the stochastic action leads to equations of motion for the optimal path connecting the boundary conditions. As we discuss in Methods, this corresponds to optimizing the total path probability between the states. Because the experiment operates in the x–z plane of the Bloch sphere, the (deterministic) equations of motion for the optimized path are
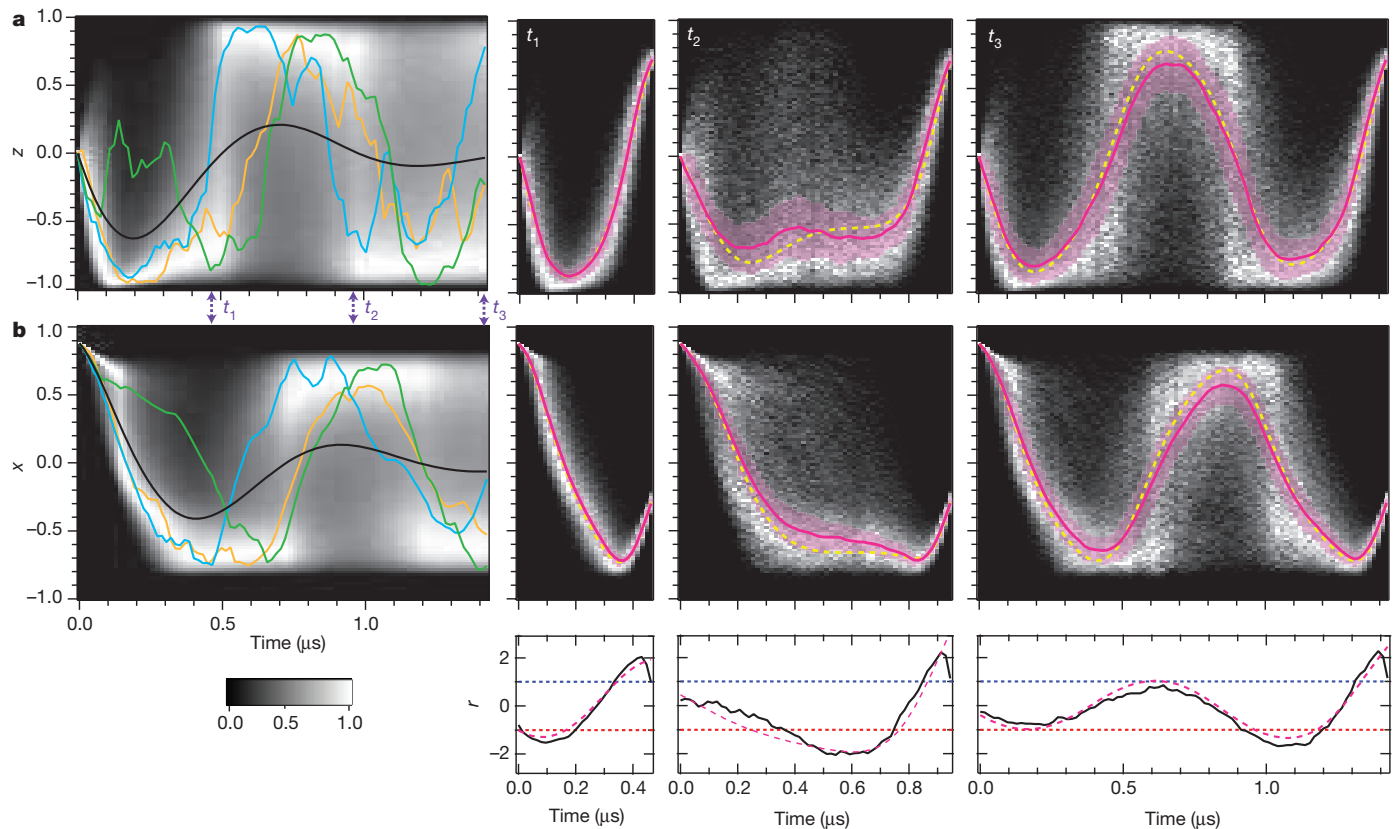
$$\dot{x} = -\gamma x + \Omega z - xzr/\tau \tag{1}$$

$$\dot{z} = -\Omega x + (1-z^2)r/\tau \tag{2}$$

$$\dot{p}_x = +\gamma p_x + \Omega p_z + p_x zr/\tau \tag{3}$$

$$\dot{p}_z = -\Omega p_x + (p_x x + 2p_z z - 1)r/\tau \tag{4}$$

where x, z, p_x, p_z and r are now functions of time (with a dot denoting a time derivative) and $r = z + p_z(1 - z^2) - p_x xz$. Here r is the optimal readout and relates to the optimal detector signal as follows: $V_{opt} = \Delta V r/2$. This rescaling makes r an estimation of z without post-selection (that

Figure 4 | Greyscale histograms of quantum trajectories in the driven case. The measurements begin at state $(x_I = 0.88, z_I = 0)$. Here $\tau = 315$ ns, $\Gamma = 3.85 \times 10^6\ s^{-1}$, $\Omega/2\pi = 1.08$ MHz. **a, b**, Histograms for z (**a**) and x (**b**) with representative trajectories plotted in colour and with the average trajectory shown in black. In the other panels in **a** and **b**, we post-select on the final state $(z_F = 0.7, x_F = -0.29)$, with a post-selection window of ± 0.08. Solid magenta curves are the most likely trajectories for the experimental data, and the yellow dashed curves are from the theory. The standard deviations of the

experimentally determined most likely paths are shown by magenta bands. As the time duration between the boundary conditions is increased from $t_1 = 0.464$ μs to $t_2 = 0.944$ μs and then to $t_3 = 1.424$ μs, the most likely trajectory connecting the initial and final states changes drastically but is well described by the theory (dashed line). The bottom panels compare the optimal detector signals (r; dashed lines) with the conditioned average signal (weak functions; black lines).

is, $p_x = p_z = 0$). The solution to these nonlinear equations admits four constants of motion, which permits the imposition of both initial (x_I, z_I) and final (x_F, z_F) boundary conditions.

The equations have a simple analytic solution $(\bar{x}, \bar{z})$ for $\Omega = 0$. We consider measurement for a time T, starting in the initial state $(x_I = 1, z_I = 0)$ and ending in a state (x_F, z_F) (in this particular case, x_F is determined by the choice of z_F). The solution of equations (1)–(4) is $(\bar{x}(t) = e^{-\gamma t} \operatorname{sech}(\bar{r}t/\tau), \bar{z}(t) = \tanh(\bar{r}t/\tau))$, where $\bar{r} = (\tau/T)\tanh^{-1}(z_F)$ is the detector output of maximum likelihood. These solutions are plotted in Fig. 3, showing agreement with the experimentally obtained most likely path (Methods). The most likely times between different boundary conditions are shown in Methods and Extended Data.

In Fig. 4, we display the full ensembles and post-selected ensembles for the driven case ($\Omega/2\pi = 1.08$ MHz). Depending on the amount of time between the initial and final states, the competition between measurement and Schrödinger dynamics produces different (and non-trivial) optimal routes, alternatively showing diffusive Rabi oscillation dynamics and quantum jump dynamics[6,24,29,30] (where the system is effectively pinned in one of the eigenstates). We compare the experimentally determined most likely trajectories (Methods) with the most likely paths obtained from solving equations (1)–(4). The equations were numerically solved with a shooting method to satisfy both initial and final boundary conditions at different times. These numerical solutions show reasonable agreement with the experimentally determined most likely curves.

In addition to the quantum paths, the solution of equations (1)–(4) also gives the optimal detector response for moving the quantum system to the target state after a given time. We compare these optimal signals to the conditioned average detector signals (weak functions) in Fig. 4. The post-selection allows the conditioned average detector signal r to exceed the usual range of $[-1, 1]$ for z. This behaviour is analogous to that of weak values, which can also lie outside their eigenvalue range[27].

The ability to find and verify the most likely path between chosen initial and final quantum states under continuous measurement extends our fundamental understanding of quantum measurement and advances the field of quantum control of individual systems. Our results give deep insight into the quantum dynamics and associated measurement read-out, as revealed by the ability to condition on the final quantum state in the presence of a continuous coherent Rabi drive. The data presented here are in good agreement with our stochastic path integral formalism, predicting the global most likely path, and open the way to solving related optimization problems important to controlling a quantum system. Examples of future applications of this approach, in the specific area of superconducting qubits, include using the continuous measurement results for improved state preparation, state estimation and Hamiltonian parameter estimation. Multiple-qubit architectures can also be fabricated, with each qubit having its own measurement device, enabling optimal continuous control protocols for an ensemble of superconducting qubits with real-time state monitoring. Furthermore, the present work can be extended to solve more general optimization problems in quantum mechanics, such as finding the most likely path from a separable state to a desired entangled state.

Online Content Methods, along with any additional Extended Data display items and Source Data, are available in the online version of the paper; references unique to these sections appear only in the online paper.

1. Vandersypen, L. M. K. & Chuang, I. L. NMR techniques for quantum control and computation. *Rev. Mod. Phys.* **76**, 1037–1069 (2005).
2. Shapiro, M. & Brumer, P. *Quantum Control of Molecular Processes* (Wiley, 2012).
3. Carmichael, H. *An Open Systems Approach to Quantum Optics* (Springer, 1993).
4. Carmichael, H. J., Kochan, P. & Tian, L. in *Proc. Int. Symp. Coherent States: Past, Present, and Future* (eds Feng, D. H, Strayer, M. R. & Klauder, J. R.) 75–91 (World Scientific, 1994).
5. Wiseman, H. & Milburn, G. *Quantum Measurement and Control* (Cambridge Univ. Press, 2010).
6. Chantasri, A., Dressel, J. & Jordan, A. N. Action principle for continuous quantum measurement. *Phys. Rev. A* **88**, 042110 (2013).
7. Guerlin, C. et al. Progressive field-state collapse and quantum non-demolition photon counting. *Nature* **448**, 889–893 (2007).
8. Sayrin, C. et al. Real-time quantum feedback prepares and stabilizes photon number states. *Nature* **477**, 73–77 (2011).
9. Hatridge, M. et al. Quantum back-action of an individual variable-strength measurement. *Science* **339**, 178–181 (2013).
10. Vijay, R. et al. Stabilizing Rabi oscillations in a superconducting qubit using quantum feedback. *Nature* **490**, 77–80 (2012).
11. Blok, M. et al. Manipulating a qubit through the backaction of sequential partial measurements and real-time feedback. *Nature Phys.* **10**, 189–193 (2014).
12. de Lange, G. et al. Reversing quantum trajectories with analog feedback. *Phys. Rev. Lett.* **112**, 080501 (2014).
13. Murch, K. W., Weber, S. J., Macklin, C. & Siddiqi, I. Observing single quantum trajectories of a superconducting qubit. *Nature* **502**, 211–214 (2013).
14. Jordan, A. N. Watching the wavefunction collapse. *Nature* **502**, 177–178 (2103).
15. Groen, J. P. et al. Partial-measurement backaction and nonclassical weak values in a superconducting circuit. *Phys. Rev. Lett.* **111**, 090506 (2013).
16. Campagne-Ibarcq, P. et al. Observing interferences between past and future quantum states in resonance fluorescence. *Phys. Rev. Lett.* **112**, 180402 (2014).
17. Ristè, D. et al. Deterministic entanglement of superconducting qubits by parity measurement and feedback. *Nature* **502**, 350–354 (2013).
18. Roch, N. et al. Observation of measurement-induced entanglement and quantum trajectories of remote superconducting qubits. *Phys. Rev. Lett.* **112**, 170501 (2014).
19. Koch, J. et al. Charge-insensitive qubit design derived from the Cooper pair box. *Phys. Rev. A* **76**, 042319 (2007).
20. Paik, H. et al. Observation of high coherence in Josephson junction qubits measured in a three-dimensional circuit QED architecture. *Phys. Rev. Lett.* **107**, 240501 (2011).
21. Castellanos-Beltran, M. A., Irwin, K. D., Hilton, G. C., Vale, L. R. & Lehnert, K. W. Amplification and squeezing of quantum noise with a tunable Josephson metamaterial. *Nature Phys.* **4**, 929–931 (2008).
22. Hatridge, M., Vijay, R., Slichter, D. H., Clarke, J. & Siddiqi, I. Dispersive magnetometry with a quantum limited SQUID parametric amplifier. *Phys. Rev. B* **83**, 134501 (2011).
23. Korotkov, A. N. Quantum Bayesian approach to circuit QED measurement. Preprint at http://arxiv.org/abs/1111.4016 (2011).
24. Korotkov, A. N. Continuous quantum measurement of a double dot. *Phys. Rev. B* **60**, 5737–5742 (1999).
25. Watanabe, S. Symmetry of physical laws. Part III. prediction and retrodiction. *Rev. Mod. Phys.* **27**, 179–186 (1955).
26. Aharonov, Y., Bergmann, P. G. & Lebowitz, J. L. Time symmetry in the quantum process of measurement. *Phys. Rev.* **134**, B1410–B1416 (1964).
27. Aharonov, Y., Albert, D. Z. & Vaidman, L. How the result of a measurement of a component of the spin of a spin-1/2 particle can turn out to be 100. *Phys. Rev. Lett.* **60**, 1351–1354 (1988).
28. Williams, N. S. & Jordan, A. N. Weak values and the Leggett-Garg inequality in solid-state qubits. *Phys. Rev. Lett.* **100**, 026804 (2008).
29. Vijay, R., Slichter, D. H. & Siddiqi, I. Observation of quantum jumps in a superconducting artificial atom. *Phys. Rev. Lett.* **106**, 110502 (2011).
30. Gambetta, J. et al. Quantum trajectory approach to circuit QED: quantum jumps and the Zeno effect. *Phys. Rev. A* **77**, 012112 (2008).

Author Contributions S.J.W. and K.W.M. performed the experiment and analysed the experimental data. J.D. and A.C. wrote the trajectory simulation code. A.C., J.D. and A.N.J. contributed the theory. All work was carried out under the supervision of I.S. All authors contributed to writing the manuscript.

METHODS

Device parameters. The qubit consists of two aluminium paddles connected by a double-angle-evaporated aluminium SQUID deposited on double-side-polished silicon. The qubit is characterized by a charging energy $E_c/h = 200$ MHz and a Josephson energy $E_J/h = 11$ GHz. The qubit is operated with negligible flux threading the SQUID loop with a transition frequency $\omega_q/2\pi = 4.01057$ GHz. The qubit is located off centre of a 6.8316 GHz copper waveguide cavity. With the measurement tone on, the qubit transition frequency was a.c.-Stark shifted to 4.00748 GHz. Qubit pulses and drive are performed at the a.c.-Stark-shifted frequency.

The lumped-element Josephson parametric amplifier (LJPA) consists of a two-junction SQUID, formed from 2 µA Josephson junctions shunted by 3 pF of capacitance, and is flux biased to provide 20 dB of gain at the cavity resonance frequency. The LJPA is pumped by two sidebands equally spaced 300 MHz above and below the cavity resonance.

Experimental set-up. Extended Data Fig. 1 displays a schematic of the experimental set-up. Experimental sequences start with an 800 ns readout to herald the $|0\rangle$ state ($z = +1$), followed by a 16 ns $\pi/2$-rotation about the y axis to prepare the qubit along the x axis. The state preparation fidelity is 88% for the data shown in Figs 2 and 4, and is 97% for the data shown in Fig. 3. After a period of variable duration, we perform quantum state tomography by applying either rotations about the x and y axes, or no rotation followed by a second 800 ns readout. Tomography results were corrected for the readout fidelity of 95%.

Calibration of the measurement. We calibrate the characteristic measurement time τ by examining histograms of the measurement signal for the qubit prepared in either the $|0\rangle$ or the $|1\rangle$ state. We prepare these states through a herald readout and then digitize the measurement signal for a variable period of time. The resulting distributions are approximately Gaussian:

$$P(V|0) = \sqrt{\frac{1}{2\pi\sigma^2}} e^{-\frac{1}{2\sigma^2}(V-\Delta V/2)^2}$$

$$P(V|1) = \sqrt{\frac{1}{2\pi\sigma^2}} e^{-\frac{1}{2\sigma^2}(V+\Delta V/2)^2}$$

We fit the distributions to determine ΔV, the voltage separation of the peaks and the variance σ^2. The quantity $S = \Delta V^2/\sigma^2$ increases linearly with integration time: $S = 4t/\tau$. We fit this relationship to determine the characteristic measurement time τ.

To calibrate the initial state and the total dephasing rate, we prepare the qubit along the x axis and perform quantum state tomography after a variable period of time. The tomography results for the full ensemble are shown in Fig. 2a, and exhibit exponential decay of coherence at rate Γ. The total quantum measurement efficiency is given by $\eta_{tot} = 1/2\Gamma\tau$. Note that the total quantum measurement efficiency $\eta_{tot} = \eta_{col}\eta_{amp}\eta_{env}$ is the product of the efficiencies for collection, for amplification and from extra environmental dephasing. We use the tomography value at $t = 0$ to determine the initial state, denoted (x_0, z_0).

To determine the Rabi frequency, Ω, we examine the ensemble tomography results as shown in Fig. 2b, c. The ensemble evolution is given by the Lindblad equation with arbitrary Rabi drive: $\dot{x}(t) = -\Gamma x(t) + \Omega z(t)$, $\dot{z}(t) = -\Omega x(t)$. With initial state (x_0, z_0), these equations have an analytic solution

$$x(t) = e^{-\Gamma t/2}\left(x_0\cos(\lambda t) - \frac{\Gamma x_0 - 2\Omega z_0}{2\lambda}\sin(\lambda t)\right)$$

$$z(t) = e^{-\Gamma t/2}\left(z_0\cos(\lambda t) + \frac{\Gamma z_0 - 2\Omega x_0}{2\lambda}\sin(\lambda t)\right) \tag{5}$$

where $\lambda = \sqrt{\Omega^2 - (\Gamma/2)^2}$. We use equation (5) to determine the Rabi frequency Ω for each measurement strength and Rabi drive amplitude.

Propagation of the qubit-state density matrix. Given the Rabi frequency Ω, the coherence decay rate γ and the initial qubit state calculated from the values of x_0 and z_0 at time $t = 0$, we propagate the initial state to states at later time steps $t = dt, 2dt, \ldots, ndt$ using a two-step procedure. At any time t, we first apply a unitary rotation to account for the Rabi drive

$$\rho'_{01} = \rho_{01} + \frac{\Omega}{2}(\rho_{00} - \rho_{11})dt \tag{6}$$

$$\rho'_{11} = \rho_{11} + \frac{\Omega}{2}(\rho'_{01} + \rho'_{10})dt \tag{7}$$

where ρ_{00}, ρ_{01}, ρ_{10} and ρ_{11} are matrix elements of a qubit density matrix $\rho(t)$. With the input values ρ'_{01} and ρ'_{11}, we next apply the Bayesian update to them based on the measurement result obtained in the time interval between t and $t + dt$, and get

$$\rho_{11}(t+dt) = \frac{(\rho'_{11}/\rho'_{00})\exp(-4V(t)dt/\tau\Delta V)}{1+(\rho'_{11}/\rho'_{00})\exp(-4V(t)dt/\tau\Delta V)} \tag{8}$$

$$\rho_{01}(t+dt) = \rho'_{01}\frac{\sqrt{(1-\rho_{11}(t+dt))\rho_{11}(t+dt)}}{\sqrt{(1-\rho'_{11})\rho'_{11}}}e^{-\gamma dt} \tag{9}$$

We use $dt = 16$ ns as the data sampling interval, and $V(t)$ is the measurement result obtained between t and $t + dt$. As discussed in the main text, we validate the state update procedure using conditioned quantum state tomography and find good agreement between individual trajectories and the tomographic reconstructions.

Moreover, in the time-continuum limit $dt \to 0$, we can approximate the state update procedure (equations (6)–(9)) with the differential equations

$$\dot{x}(t) = -\gamma x(t) + \Omega z(t) - x(t)z(t)r(t)/\tau \tag{10}$$

$$\dot{z}(t) = -\Omega x(t) + (1-z(t)^2)r(t)/\tau \tag{11}$$

where $r(t) = 2V(t)/\Delta V$ is the dimensionless measurement signal, and $x(t) = \mathrm{tr}[\sigma_x\rho(t)]$ and $z(t) = \mathrm{tr}[\sigma_z\rho(t)]$ are the Bloch vector coordinates as functions of time.

Tomographic validation. To verify that we have accurately tracked the quantum state of the system, we perform quantum state tomography at discrete times along the trajectory. We denote the target trajectory, which is based on a single run of the experiment, $(\tilde{x}(t), \tilde{z}(t))$ For each experimental sequence of total measurement duration t, we propagate ρ and, if $x(t) = \tilde{x}(t) \pm 0.03$ and $z(t) = \tilde{z}(t) \pm 0.03$, then the subsequent tomography results are included in the tomographic reconstruction of the state at time t. We repeat this analysis for all time steps between 0 and 1.6 µs, and find good agreement between the individual trajectories and the tomographic reconstructions.

Histogram scaling. The greyscale histograms shown in Figs 3 and 4 represent the values of x and z at each time point, binning with the bin size of 0.02. The greyscale shading is normalized such that the most frequent value is 1 at each time point.

Derivation of the ordinary differential equations in equations (1)–(4). We consider a set of unitless measurement readouts $\{r_k\} = \{r_0, r_1, \ldots, r_{n-1}\}$, where $r_k = 2V_k/\Delta V$, at times $\{t_k = kdt\}$ for $k = 0, 1, \ldots, n-1$, and its corresponding set of qubit states, denoted $\{q_k\}$. In our experiment, the y component of the qubit Bloch coordinates is always zero, and q_k is thus a two-dimensional vector: $q_k = (x_k, z_k)$. We write a joint probability density function of all measurement outcomes $\{r_k\}$, the quantum states $\{q_k\}$ and the chosen final state q_F, conditioned on the initial state q_I as

$$P(\{q_k\},\{r_k\},q_F|q_I) = \delta^2(q_0-q_I)\delta^2(q_n-q_F)$$
$$\times\left(\prod_{k=0}^{n-1}P(q_{k+1}|q_k,r_k)P(r_k|q_k)\right) \tag{12}$$

Here $P(q_{k+1}|q_k, r_k)$ is a probability density function of a qubit state at time t_{k+1} given a qubit state and measurement signal at previous time t_k. Because a qubit state at any time t_{k+1} is updated deterministically from q_k and r_k, the density function $P(q_{k+1}|q_k, r_k)$ is a delta function whose argument imposes the state update equations. The conditional distribution of the detector output $P(r_k|q_k)$ obtained in a time interval dt is a probability density function of r_k given q_k:

$$P(r_k|q_k) = \sqrt{\frac{dt}{2\pi\tau}}\left(\frac{1+z_k}{2}e^{-\frac{dt}{2\tau}(r_k-1)^2} + \frac{1-z_k}{2}e^{-\frac{dt}{2\tau}(r_k+1)^2}\right)$$

By expressing the delta functions in equation (12) in Fourier-transformed forms with conjugate variables $p_k = (p_k^x, p_k^z)$ for $k = -1, 0, \ldots, n$ and other terms in exponential form, we can write the joint probability density function in a path integral representation $P(\{q_k\},\{r_k\},q_F|q_I) \propto \int \mathcal{D}p\, e^{\mathcal{S}}$. Here $\mathcal{D}p$ is an integral measure over conjugate variables $\{p_k\}$, and $\mathcal{S}$ is an action given by

$$\mathcal{S} = -p_{-1}\bullet(q_0-q_I) - p_n\bullet(q_n-q_F)$$
$$+ \sum_{k=0}^{n-1}\{-p_k\bullet(q_{k+1}-\mathcal{E}[q_k,r_k]) + \ln P(r_k|q_k)\} \tag{13}$$

$$= -B + \int_0^T dt[-p_x\dot{x} - p_z\dot{z} + p_x(-\gamma x + \Omega z - xzr/\tau)$$
$$+ p_z(-\Omega x + (1-z^2)r/\tau)$$
$$- (r^2 - 2rz + 1)/2\tau] \tag{14}$$

where we have used the operator $\mathcal{E}[q_k, r_k]$ to indicate the state update, and B as a short-hand for the first two terms in equation (13). We note that, in equation (14), we have taken the time-continuum limit $dt \to 0$ and written the action explicitly

for our qubit measurement case with the state update equations (10) and (11). We have also used shortened notation for the variables, for example $x = x(t) \equiv \lim_{dt \to 0} \{x_0, x_1, \ldots, x_n\}$. To obtain the most likely path, we then extremize the action in equation (14) over all variables (x, z, p_x, p_z, r) and obtain the ordinary differential equations (ODEs) shown in equations (1)–(4):

$$\dot{x} = -\gamma x + \Omega z - xz \, r/\tau \qquad (15)$$

$$\dot{z} = -\Omega x + (1 - z^2) r/\tau \qquad (16)$$

$$\dot{p}_x = +\gamma p_x + \Omega p_z + p_x z \, r/\tau \qquad (17)$$

$$\dot{p}_z = -\Omega p_x + (p_x x + 2 p_z z - 1) r/\tau \qquad (18)$$

Here $r = z + p_z(1 - z^2) - p_x xz$ and the forced boundary conditions are $x(t = 0) = x_I$, $z(t = 0) = z_I$, $x(t = T) = x_F$, $z(t = T) = z_F$. As discussed in the main text, we can analytically solve the ODEs in equations (15)–(18) when $\Omega = 0$. For the driven case, where $\Omega \neq 0$, we solve the equations numerically using a shooting method.

Interpretation of the solutions of the ODEs. Here we discuss the interpretation of the solution of the ODEs in equations (15)–(18) (and equations (1)–(4)). The extremization of the action in equation (13) can also be interpreted as a constrained optimization of the last term of equation (13), $\sum_{k=0}^{n-1} \ln P(r_k|q_k)$, which is the log-likelihood of the trajectory. The constraints are as follows: (1) the qubit state updates $q_{k+1} = \mathcal{E}[q_k, r_k]$ for $k = 0, 1, \ldots, n - 1$; (2) the pre-selected state is $q_0 = q_I$; and (3) the post-selected state is $q_n = q_F$. The conjugate variables $\{p_k\}$ now act as the Lagrange multipliers of the constrained optimization. With this interpretation, a solution of the ODEs in equations (15)–(18) therefore represents a path with an optimized value of $\sum_{k=0}^{n-1} \ln P(r_k|q_k)$ or its exponential $\prod_{k=0}^{n-1} P(r_k|q_k)$, that is, a measurement path probability density.

The most likely path. The optimized path mentioned in the previous subsection can represent either a maximum, a minimum or a saddle point of the path probability under the constraints. We can determine which by finding paths slightly varied from the optimized solution, with all constraints still applied. This can be done by adding small constants δ_1 and δ_2 to the right-hand sides of the differential equations of the conjugate variables p_x and p_z (equations (17) and (18)), leaving the equations for x and z unchanged, and solving the whole system with the same boundary conditions. Solutions of the modified ODEs will be slightly varied from the optimized path. We then compute their full-path probabilities, comparing with the probability calculated from the optimized path. In Extended Data Fig. 2, we show samples of paths from the variational method described here and the unnormalized full-path probability of the surrounding paths. In this case, it shows that the optimized solution is the most likely path, with a maximum value of the path probability density.

The most likely paths from the experimental post-selected trajectories. To find the most likely path from experimental trajectory data, we first define the closeness of any two trajectories (named a and b) as a time-average of the Euclidean distance:

$$D \equiv (1/n) \sum_{k=0}^{n-1} \sqrt{(x_a(t_k) - x_b(t_k))^2 + (z_a(t_k) - z_b(t_k))^2}$$

where $t_k = k \, dt$ and dt is the time step. For a qubit, the Euclidean distance is the trace distance (up to a factor of 2) between two quantum states ρ_1 and ρ_2, given by $(1/2)\mathrm{tr}[\rho_1 - \rho_2]$. We compute the distance D between all possible pairs of trajectories starting from the same initial state $q_I = (x_I, z_I)$ and ending around a final state $q_F = (x_F, z_F)$ with a small tolerance. We then search for N trajectories that have minimum average distance to all others, and average them to obtain an estimate of the most likely path. The number of trajectories N is chosen to be about 10% of the total number of trajectories in the sub-ensemble. (N is of order 10^2, compared with 10^3 trajectories in the sub-ensemble). As a result, we get a smooth estimate of the most likely path, which is still very different from the total (sub-ensemble) averaged trajectory. We plot the standard deviation of the data of x and z for the chosen 10% of trajectories for every time step as a shaded band in Figs 3 and 4. As shown in those figures, the experimentally determined most likely paths closely approximate the theoretical most likely paths, that is, the solutions of the ODEs in equations (15)–(18). We expect that the approximated curves converge to the smooth theory curves in the limit of an infinite ensemble of post-selected trajectories.

In some cases, we can simply look at a trajectory of local medians (medians of x or z at all time steps) and compare it with the theoretical most likely path. The median trajectory can in practice be a good approximation to the theory curve when the distribution of the post-selected trajectories is a narrow band, that is, when the post-selected trajectories lie closely around a single path. As an example, in the case where there is no drive on the qubit, $\Omega = 0$, we show in our theory paper[6] that the median curves agree quite well with the most likely curves. However, in the driven case where the qubit trajectories can possibly have different winding numbers around the y axis, resulting in multiple most likely paths from an initial state to a final state, simply finding the median of the distribution of x or z is not enough to capture their most likely behaviour. In this paper, we focus only on the cases where there is a single most likely path between any two boundary states. We will discuss our findings concerning the multiple paths connecting two boundary states in a future work.

The most likely time. Apart from the path of maximum likelihood taken between the pre- and post-selected states in a fixed time, a complementary problem in quantum control is that of the optimal waiting time between starting and destination states. In the case where there is no Rabi drive on the qubit, $\Omega = 0$, we can fix the states at the endpoints and inquire about the most likely time taken to travel between them. While a path integral derivation of the most likely time is possible, we give a simpler derivation here based on the probability distribution of the time-average measurement readout $V = (1/n) \sum_{k=0}^{n-1} V_k$.

In the case with no drive on the qubit, the z coordinate of the qubit on the Bloch sphere at any time T is solely determined by V. We can derive the distribution of the final z coordinate (z_F) at any time T, given the initial z coordinate (z_I), $P(z_F|z_I)$, from the probability density function $P(V|z_I)$. The probability density function of V, given z_I, is

$$P(V|z_I) = P(V|0)\frac{1 + z_I}{2} + P(V|1)\frac{1 - z_I}{2}$$

$$= \sqrt{\frac{1}{2\pi\sigma^2}}\left(\frac{1 + z_I}{2} e^{-\frac{1}{2\sigma^2}(V - \Delta V/2)^2} + \frac{1 - z_I}{2} e^{-\frac{1}{2\sigma^2}(V + \Delta V/2)^2}\right)$$

where the variance of the voltage signal measured in a time dt is $\sigma^2 = \Delta V^2 \tau/4dt$. We change variable from the time-averaged measurement signal V to the final z component z_F as follows: $V = (\tau \Delta V/2T)\left[\tanh^{-1}(z_F) - \tanh^{-1}(z_I)\right]$. We obtain the differential measure $dV = (\tau/2T)\left[\Delta V/(1 - z_F^2)\right]dz_F$. The probability density function of z_F given z_I can be computed via the relation $P(V|z_I)dV = P(z_F|z_I)dz_F$:

$$P(z_F|z_I) = \frac{\sqrt{\tau/2\pi T}}{(1 - z_F^2)} \times \exp\left\{-\frac{T}{2\tau}(\bar{r}^2 + 1) + \frac{1}{2}\ln\left(\frac{1 - z_I^2}{1 - z_F^2}\right)\right\}$$

where $\bar{r} \equiv \frac{\tau}{T}\tanh^{-1}\left(\frac{z_F - z_I}{1 - z_I z_F}\right) = \frac{\tau}{T}\left(\tanh^{-1}(z_F) - \tanh^{-1}(z_I)\right)$. For the case where the initial state is $x = +1$ ($z_I = 0$), the probability density function simplifies to

$$P(z_F|z_I = 0) = \frac{\sqrt{\frac{\tau}{2\pi T}}}{(1 - z_F^2)^{\frac{3}{2}}}\exp\left\{-\frac{T}{2\tau} - \frac{\tau}{2T}[\tanh^{-1}(z_F)]^2\right\}$$

We then compute the most likely time T_{opt} where the probability density function $P(z_F|z_I)$ is maximized for the fixed values of z_I and z_F. By maximizing the probability function $P(z_F|z_I)$ with respect to T, we obtain

$$T_{opt} = \tau\left(\frac{\sqrt{1 + 4\bar{\gamma}^2} - 1}{2}\right)$$

where $\bar{\gamma} \equiv \tanh^{-1}\left(\frac{z_F - z_I}{1 - z_I z_F}\right)$. We show in Extended Data Fig. 3 the distributions $P(z_F|z_I = 0)$ as a function of time T for $z_F = 0.2, 0.4, 0.6$. They show very good agreement with the experimental data.
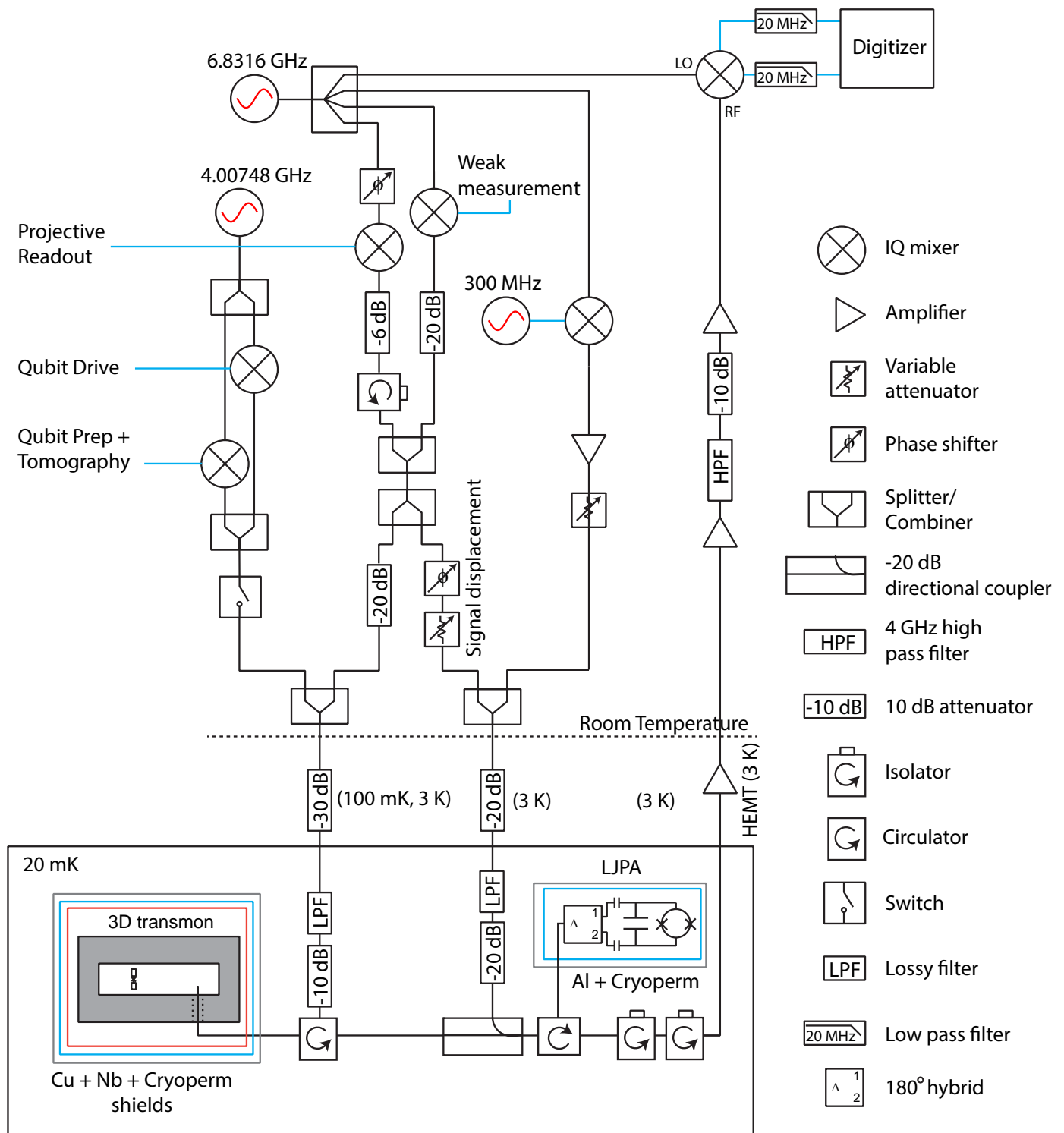
Extended Data Figure 1 | Experimental schematic. The weak measurement tone is always on. The projective readout tone is pulsed. The amplitude and phase of the signal displacement tone are adjusted to displace the measurement signals back to the origin of the X_1–X_2 plane, which allows the LJPA to perform in the linear regime.
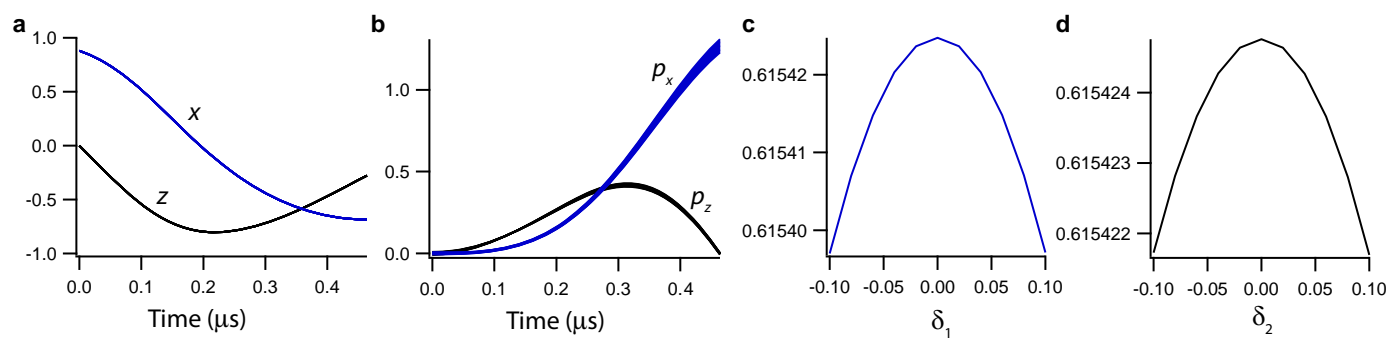
Extended Data Figure 2 | Paths slightly varied from the optimal solution.
a, Overplotted x and z coordinates of 11 trajectories slightly varied from
an optimized solution with boundary conditions $(x_\mathrm{I}, z_\mathrm{I}) = (0.88, 0)$,
$(x_\mathrm{F}, z_\mathrm{F}, T_\mathrm{F}) = (-0.683, -0.227, 0.464\,\mu s)$ and the Rabi drive $\Omega/2\pi = 1.08$ MHz.
**b**, The corresponding conjugate variables p_x and p_z. **c**, **d**, Plots of the
unnormalized probability versus changes of the constant δ_1 in the p_x differential
equation (**c**) and the unnormalized probability versus changes of the constant
δ_2 in the p_z differential equation (**d**). In this case, the optimized solution
gives a maximum value of the path probability density.
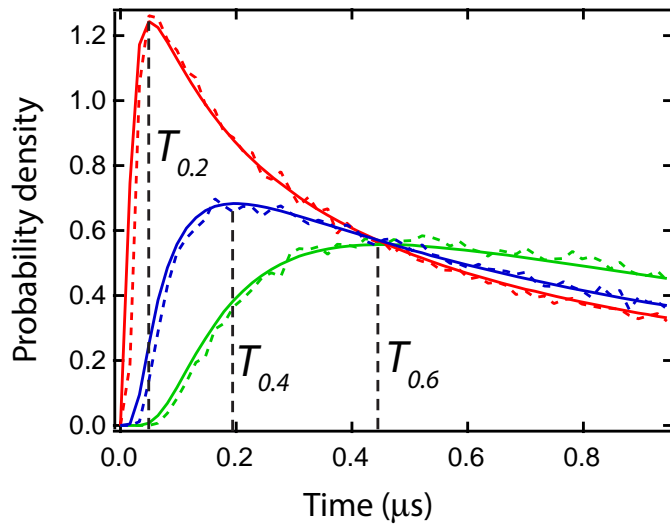
Extended Data Figure 3 | Optimal time between starting and destination states. The probability density functions $P(z_F | z_I = 0)$ plotted as functions of time T (solid curves) along with experimental data (dotted curves) with $\tau = 1.25 \,\mu s$. The red, green and blue curves are the distribution functions $P(z_F = 0.2 | z_I = 0)$, $P(z_F = 0.4 | z_I = 0)$ and $P(z_F = 0.6 | z_I = 0)$, respectively. The optimized times T_{opt} for the three cases are shown as the vertical black dashed lines with the labels $T_{0.2}$, $T_{0.4}$ and $T_{0.6}$.
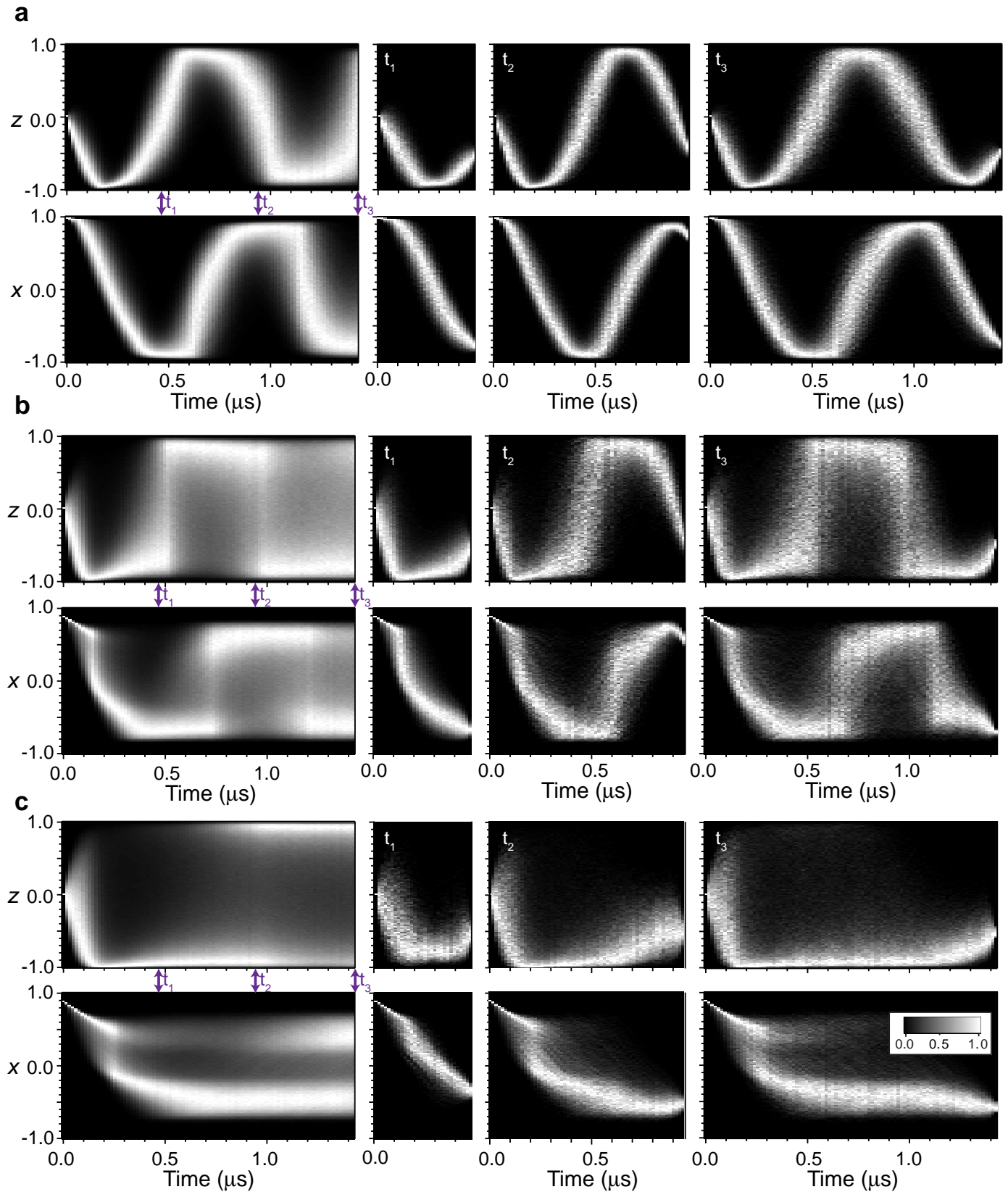
Extended Data Figure 4 | Greyscale histograms of ensemble and post-selected trajectories for different Rabi frequencies and measurement strengths. a, Ensemble and post-selected trajectories for $\Omega/2\pi = 1.08$ MHz and $\tau = 1.25$ μs. The post-selections for times {$t_1 = 464$ ns, $t_2 = 944$ ns, $t_3 = 1.424$ μs} are $(x_F, z_F) = \{(-0.78, -0.5), (0.7, -0.5), (-0.73, -0.5)\}$ with a post selection window of ± 0.08. **b**, Trajectories for $\Omega/2\pi = 1.08$ MHz and $\tau = 315$ ns with $(x_F, z_F) = \{(-0.69, -0.5), (0.5, -0.5), (-0.73, -0.5)\}$. **c**, Trajectories for $\Omega/2\pi = 0.58$ MHz and $\tau = 315$ ns with $(x_F, z_F) = \{(-0.35, -0.5), (-0.5, -0.5), (-0.56, -0.5)\}$. Note that all the trajectories use the same value of z_F. The values of x_F were chosen to give a large number of trajectories in the post-selected ensemble.